GDCh Research Article Angewandte International Edition Chemie www.angewandte.org

How to cite: *Angew. Chem. Int. Ed.* **2025**, *64*, e202419495
doi.org/10.1002/anie.202419495

Zinc -Ion Batteries

Sulfurized Composite Interphase Enables a Highly Reversible Zn Anode

Lu Wu[+], Hao Yuan[+], Yongkang An, Jianguo Sun, Yu Liu, Han Tang, Wei Yang, Lianmeng Cui, Jinghao Li, Qinyou An, Yong-Wei Zhang, Lin Xu,* and Liqiang Mai**

Abstract: The stability and reversibility of Zn anode can be greatly improved by in situ construction of solid electrolyte interphase (SEI) on Zn surface via a low-cost design strategy of $ZnSO_4$ electrolyte. However, the role of hydrogen bond acceptor -SO_3 accompanying ZnS formation during SEI reconstruction is overlooked. In this work, we have explored and revealed the new role of -SO_3 and ZnS in the in situ formed sulfide composite SEI (SCSEI) on Zn anode electrochemistry in $ZnSO_4$ aqueous electrolytes. Structure characterization and DFT demonstrate that the introduction of -SO_3 can not only reduce the dehydration energy of $[Zn(H_2O)_6]^{2+}$, but also enhance the stability of the ZnS/Zn interface and homogenize the ZnS/Zn interface electric field, thereby significantly improving the dynamic kinetics and uniform deposition of Zn^{2+}. Owing to the synergistic effect of ZnS and -SO_3, a high cycling stability of 1500 h with a cumulative-plated capacity of 7.5 Ah cm^{-2} at 10 mA cm^{-2} has been achieved within the symmetrical cell. Furthermore, the full cell with $NH_4V_4O_{10}$ cathode exhibits outstanding cyclic stability, exceeding 2000 cycles at 5 A g^{-1} and maintaining a Coulombic efficiency of 100 %. These new insights into anionic synergistic strategy could significantly enhance the practical application of zinc-ion batteries.

Introduction

In the paradigm shift of sustainable energy resources, aqueous Zn-metal batteries (AZMBs) emerge as a promising contender, attributed to their intrinsic merits in terms of safety, availability, and cost-friendly.[1] Nevertheless, the practical implementation of AZMBs has still faced significant hurdles originating from the unstable electrolyte–anode interface, where hydrogen evolution reactions (HERs) and corrosion reactions occur due to the high reactivity between the active water and fresh Zn anode.[2] These interactions precipitate the formation of by-product ($Zn_4SO_4(OH)_6{\cdot}xH_2O$, ZSH) and promote erratic Zn deposition, thereby accelerating dendritic growth.[3] Consequently, all the above irreversible interfacial reactions trigger the low Coulombic efficiency (CE) and deteriorate the cycling system during the plating/stripping of Zn^{2+}.[4]

To alleviate the irreversible side reaction at the electrode-electrolyte interface, it is imperative to curtail the corrosion of Zn and improve the stability of the interface.[5] Developing an in situ sulfurized solid-state electrolyte interphase stands out as a viable approach, which can guard high Zn^{2+} conductivity alongside remarkable stability and protection against active water attacks.[6] In a pioneering endeavor, Guo's group has built an artificial ZnS layer on Zn surface to enhance the Zn reversibility and facilitate dendrite-free Zn plating/stripping.[7] However, the complex manufacturing processing of vapor-solid strategy makes it difficult to ensure the uniformity and density of the ZnS layer. Compared to the ex situ artificial SEI layers, given its simplicity and cost-effectiveness, the formation of in situ SEI composite layers via electrolyte additives is regarded as a more practical methodology for large-scale energy storage.[8] For instance, Nazar et al. reported that the additive N, N-dimethylformamidium.

trifluoromethanesulfonate (DOTf) would dissociate into trifluoromethanesulfonic acid under the assistance of water,

[*] L. Wu,[+] Y. An, Y. Liu, W. Yang, L. Cui, J. Li, Prof. Q. An, Prof. L. Xu, Prof. L. Mai
State Key Laboratory of Advanced Technology for Materials Synthesis and Processing, School of Materials Science and Engineering, Wuhan University of Technology,
Wuhan, 430070, China
E-mail: linxu@whut.edu.cn
mlq518@whut.edu.cn

Dr. H. Yuan,[+] Prof. Y.-W. Zhang
Institute of High Performance Computing (IHPC), Agency for Science, Technology and Research (A*STAR), 1 Fusionopolis Way, #16-16 Connexis, Singapore 138632, Singapore
E-mail: zhangyw@ihpc.a-star.edu.sg

Dr. J. Sun
Department of Materials Science and Engineering, National University of Singapore,
Singapore 117574, Singapore

Dr. H. Tang
Hubei Provincial Key Laboratory of Green Materials for Light Industry, School of Materials and Chemical Engineering, Hubei University of Technology,
Wuhan 430068, China

Prof. L. Xu, Prof. L. Mai
Hubei Longzhong Laboratory, Wuhan University of Technology (Xiangyang Demonstration Zone),
Xiangyang 441000, China

Prof. L. Xu
Zhongyu Feima New Material Technology Innovation Center (Zhengzhou) Co., Ltd., Zhengzhou 450001, China

[+] These authors contributed equally to this work.

forming a robust nanostructure of S-containing SEI, which can efficaciously repel water and regulate the uniform deposition of Zn anode.[2b] The findings also revealed a clear formation mechanism in sulfate-based electrolytes. Nonetheless, there remains a paucity of comprehensive analyses elucidating the anionic synergistic effect of -SO_3.[3d,9] Therefore, the key components of -SO_3 in the SEI that enhance performance still need to be clarified, especially in low-cost sulfate-based electrolytes.

Herein, we construct an in situ interphase protective layer on the Zn surface via a modulating electrolyte strategy aimed at improving the electrochemical performance of the Zn anode. Through a synergistic blend of experimental analyses and theoretical computations, we find that a sulfurized composite electrolyte interphase layer (bridge -SO_3 onto ZnS layer) forms in situ on the Zn surface (SCSEI@Zn) during cycling. Such a layer like a knight valiantly positioned on the surface of Zn metal (Figure 1a), not only bolsters interface stability and curtails corrosion side reactions but also facilitates the reduction in dehydration energy of $[Zn(H_2O)_6]^{2+}$ and ensures the uniform Zn^{2+} deposition. Consequently, it promotes fast Zn ion transport kinetics and yields a dendrite-free Zn anode. In contrast, during the cycling process, the zinc anode will undergo corrosion and passivation side reactions in the electrolyte without additives, thus accumulating to form loose and porous $Zn_4(OH)SO_4{\cdot}xH_2O$ (ZSH) and zinc dendrites (Figure 1b).[10] As a result, a significantly high cumulative-plated capacity of 7.5 Ah cm^{-2} at 10 mA cm^{-2}, alongside a high average CE of 99.55 % over 1790 cycles, have been obtained in both half-cells using SCSEI@Zn anode. Moreover, a Zn || $NH_4V_4O_{10}$ incorporating the SCSEI@Zn electrode exhibits a superior cycling stability of 2000 cycles to achieve excellent performance with remarkable high Coulombic efficiency (CE ≈100 %) at 5 A g^{-1}, significantly outperforming that of using a bare Zn anode.

Results and Discussion

Given the importance of the SEI in achieving high reversibility of lithium anode in lithium metal batteries, the endeavor to engineer SEI layers for Zn anodes within aqueous electrolytes merits considerable attention.[11] Introducing additives as an efficient and cost-effective strategy can in situ form a robust SEI on the Zn anode surface and make it easier to achieve practical applications.[12] Various fluorochemical additives (Table S1), such as TFA and FEC, which can regulate the solvated structure of Zn^{2+} to reduce H_2O, further construct a high-quality and ZnF_2-riched SEI layer.[13] However, the in situ forming of fluorinated SEI in low-concentration AZIBs is of great challenge. Besides, ZnF_2 has a lower Zn^{2+} transfer number than that of the ZnS.[7,14] Therefore, forming a SEI layer dominated by ZnS is also an effective approach to provide an effective interphase. Currently, the SEI with composite components including Zn sulfide and sulfite anion can prevent corrosion and inhibit HER reduction have been reported.[2b,15] However, the key components in the SEI that enhance performance are still unclear, especially in sulfate-based electrolytes. Drawing on these insights, we attempted to in situ construct an SCSEI layer on the Zn anode surface using Flu/$ZnSO_4$ electrolyte, aiming to corroborate these findings and elucidate the impact of zinc sulfide and sulfite anion on the Zn anode in a comprehensive manner.

To investigate the composition and morphological structure of the Zn anode interface after the introduction of additives, XPS, TEM, TOF-SIMS techniques, and MD simulations were applied. XPS was carried out to investigate the surface of the Zn anode after cycling in $ZnSO_4$ electrolyte with Flu, which was tested at a depth along with the increasing time Ar^+ etching. The high-resolution spectra of S 2p region shows apparent peaks of strong SO_4^{2-} (170.18/169.0 eV), weak -SO_3 (168.1 eV), and ZnS (163.66/

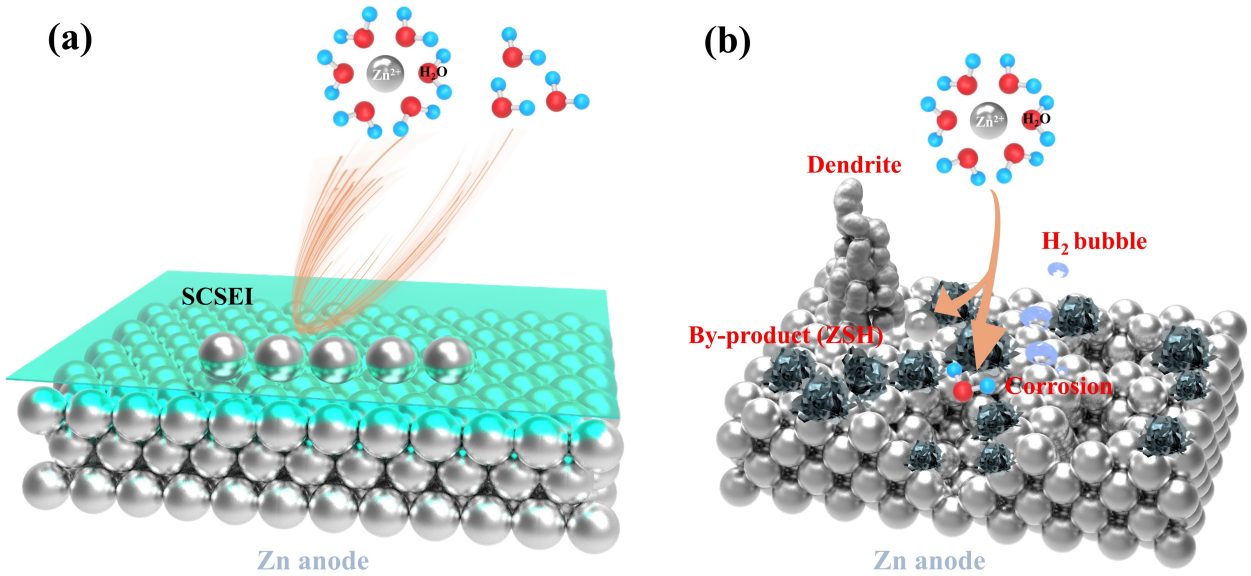

Figure 1. Schematic of Zn deposition mechanism on (a) SCSEI@Zn anode and (b) bare Zn anode.

162.11 eV) in Figure 2a.[16] The SO_4^{2-} species predominantly present on the surface of Zn anode, which are originated from the precipitation of $ZnSO_4$ electrolyte.[16] Upon further sputtering to 60 s, the content of -SO_3 and ZnS increase to 11.4 % and 27.6 %, respectively. Both -SO_3 and ZnS components may be caused by the reduction decomposition of SO_4^{2-} as previously reported.[2b,6,17] Besides, in the O 1s spectra, there is a sharp drop of the C=O content owing to the simple adsorption behavior of organic compound on Zn surface after etching the surface. In contrast, there are no ZnS and -SO_3 species that can be observed with Ar^+ sputtering depth in the bare Zn anode after cycled in bare $ZnSO_4$ electrolyte (Figure S7), it indicates that the proposed methodology with suitable additives can promote the in situ construction of SCSEI on the Zn anode surface. Meanwhile, the depth of F 1s spectra of Zn anode cycling in Flu/$ZnSO_4$ electrolyte not appear the F signal (Figure S8). In contrast, the original powder of Flu shows the obvious peak of C–F (687.6 eV) (Figure S9). These results can exclude the formation of -SO_3 through the decomposition of electrolyte additives. Both -SO_3 and ZnS components may be caused by the reduction decomposition of SO_4^{2-} as previously reported.[2b,17] The pH increases to 4.3 after the first cycle and stabilize after subsequent cycles indicates that the SEI mainly forms during the initial cycles (Figure S10). The Flu additive may be able to bind to the OH^- ions to prevent Zn passivation on Zn anode as well as the hydrogen radical (H) in situ reduced SO_4^{2-} to form sulfide composite SEI (SCSEI, bridge -SO_3 onto ZnS layer) on the Zn anode surface, thereby inhibiting the formation of ZSH by-products and H_2 bubble, which is consistent with the results of XRD, XPS and pH analysis. To verify whether the Flu additive possesses a similar effect in electrolytes with other Zn salts, Zn anodes after cycled in $Zn(CF_3SO_3)_2$ electrolyte with or without Flu additive were explored by XPS. Obvious signal of ZnS and -SO_3 were observed on the Zn anode surface after cycled in Flu-containing $Zn(CF_3SO_3)_2$ electrolyte (Figure S11), but no signal of ZnS was observed on the Zn anode surface after cycling in bare $Zn(CF_3SO_3)_2$ electrolyte (Figure S12), which is also consistent with the results of $ZnSO_4$-based electrolyte.

Following, TOF-SIMS equipped with a Ga^+ ion beam was further carried out to characterize the specific composites of SEI layer (Figure 2c).[18] For Zn anode after cycled

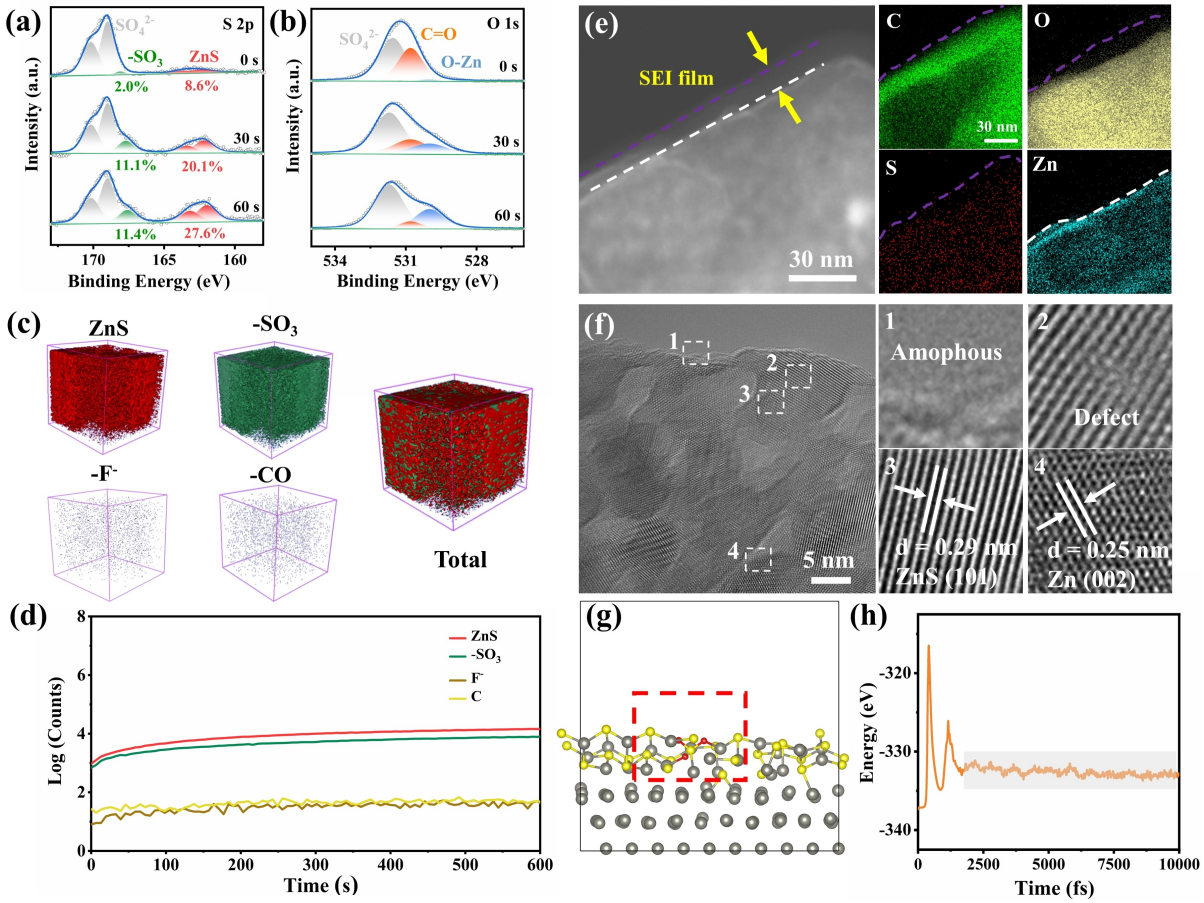

Figure 2. Characterization of SEI chemistry. The XPS depth profile of (a) S 2p and (b) O 1s. (c) The 3D visualization of TOF-SIMS intensity related to the corresponding charged fragments. (d) Depth profile curves of TOF-SIMS in negative mode (e) TEM image, HAADF image and corresponding elemental mapping of the sample. (f) HRTEM images of typical four areas, along with the partially enlarged images of the marked areas. (g) MD simulations of an elevation view of 3D snapshot at the time of 10 ps of the ZnS@SO_3 system. (h) Time-dependent energy of ZnS@SO_3 system.

in Flu-containing $ZnSO_4$ electrolyte, Three-dimensional (3D) visualization shows the content of ZnS and -SO_3 gradually increases with depth etching of 600 s (Figure 2d), which firmly verifies that the SCSEI layer formed on the Zn anode surface is a ZnS@SO_3 hybrid interphase. For Zn anode after cycling in bare $ZnSO_4$ electrolyte, 3D visualization shows the obvious content of OH^- species, which corresponds to the by-product. The signal of ZnS and -SO_3 is apparently weaker than that of cycling in Flu/$ZnSO_4$ (Figure S13), verifying that the main components of the SEI are OH^- fragment originated from the ZSH.

To further analyze the morphology and structure of SEI, we prepared the Zn metal-coated copper grid anode in ZnSO4 and Flu/$ZnSO_4$ electrolyte to reappear above samples for TEM characterization (Figure S14). In Flu/$ZnSO_4$ electrolyte system, a representative ultrathin film at the Zn metal surface can be observed from the high-angle annular dark-field (HAADF) images (Figure 2e). The energy dispersive X-ray spectroscopy (EDX) mapping images show the homogeneous elements distribution (C, O, S, Zn). The presence of Zn is observed at in the center of the particle (in the white dotted line), and C, O, S elements are uniformly distributed in the entire particle surface (in the purple dotted line), which further verifies the existence of an ultrathin SCSEI layer that is composed of sulfate anion and Flu reduction products during the Zn disposition process. Furthermore, as shown in the four typical regions in the high-resolution TEM (HRTEM) images (Figure 2f), interestingly, distinct vacancies are observed in the region of amorphous SEI in the second area, which further confirms that the SEI comprises two substances: -SO_3 and ZnS. Moreover, the layer spacings at the edges can correspond to the (101) lattice plane of ZnS (0.29 nm) and the (002) lattice plane of Zn (0.25 nm), respectively. The -SO_3 may represent zinc sulfite salts or a group that bridges the ZnS surface. Considering that zinc sulfite salts are difficult to exist stably in weakly acidic $ZnSO_4$ electrolytes, the sulfurized composite formed by bonding of oxygen atoms in -SO_3 with Zn atoms in ZnS is a very possible form of existence. This evidence clearly indicates that the SCSEI layer has formed and comprises anion species along with ZnS@SO_3. In the bare $ZnSO_4$ electrolyte system, the HRTEM images showed the lattice fringe with an interplanar spacing of approximately 0.364 nm, which is consistent with the (003) plane of ZSH (Figure S15). The aforementioned findings indicate that that the ZSH is the main stable component of the SEI-like layer which is formed on the Zn anode in $ZnSO_4$ electrolyte.

The stability of ZnS@SO_3 composite structure on the Zn surface was first studied through MD simulations. The initial state in the composite interface layer of ZnS@SO_3 system is shown in Figure S16. From the 3D snapshot of the elevation and vertical views of ZnS@SO_3 (Figure 2g and Figure S17, respectively), it can be found that the "oxygen ferry" originated from -SO_3 between ZnS and Zn^{2+} can capture Zn^{2+} through the formation of O and Zn^{2+} coordination. The 3D snapshots for the final state of ZnS@SO_3 system are taken at 10 ps. The detailed energy change process is shown in Figure 2h. After 1500 fs equilibrium of MD simulations, the system energy stabilizes at approximately −332 eV and this equilibrium state persists until 10000 fs, confirming the critical role of the -SO_3 coating interaction formed at the in situ SCSEI of ZnS@SO_3 composite in enhancing stability. This can be attributed to the high structure stability observed in the MD simulation over an extended simulation period. It can be inferred that the stability of the ZnS@SO_3 increases with aging time. Furthermore, the results of 3D snapshots and system energy curve of ZSH@Zn at initial and after 10 ps indicate that ZSH by-products can maintain stability on the surface of zinc anode (Figures S18–S20). Impressively, the contact angle between bare Zn and the electrolyte measures 112°, in contrast to 79° between Zn and Flu electrolyte (Figure S21). This comparison illustrates that Flu can effectively improve zincophilicity and ensure the formation of SCSEI interphase layer.

The stability and reversibility of the Zn^{2+} plating/stripping on bare Zn and SCSEI@Zn were further investigated in half cells. The SCSEI@Zn displays a long-term cyclic stability of 2800 h compared with the bare Zn (cycling lifetime of 360 h) in the symmetrical batteries under a constant current density of 1 mA cm^{-2} with an area capacity of 1 mAh cm^{-2} (Figure 3a). Even under the conventional capacity condition (5 mA cm^{-2} and 5 mAh cm^{-2}),[19] the cell with SCSEI@Zn electrode can still possess 280 h stable cycles (Figure 3b), which can be attributed to the excellent Zn^{2+} stability and reversibility owing to the SCSEI layer. Moreover, the rate performance testing displays an impressive flat voltage profile and a small voltage hysteresis of SCSEI@Zn electrode from 0.5 mA cm^{-2} to 15 mA cm^{-2}, then back to 0.5 mA cm^{-2} (Figure 3c). Notably, a cumulative plated capacity of 7.5 Ah cm^{-2} can be achieved at a high current density of 10 mA cm^{-2} over 1500 h (Figure 3d), Even at current densities up to 20 mA cm^{-2}, the Zn//Zn symmetric cell using SCSEI@Zn anode can be stable for 2500 cycles (Figure S22). These results indicate that SCSEI@Zn anode exhibits significantly improved stability compared to bare Zn anode.

Furthermore, the ZnS@Zn electrode is obtained after several cycles in the Flu/$ZnSO_4$ electrolyte and disassembled and cleaned several times, and then the symmetrical cells have been assembled in the $ZnSO_4$ electrolyte to evaluate whether the in situ formation of ZnS@SO_3 SEI goes beyond the pure ZnS. The pure ZnS electrode can well run over 1040 h at a current density of 1 mA cm^{-2} and 1 mAh cm^{-2} (Figure S23), but does not break through the electrochemical performance of SCSEI@Zn electrode in the present research, it indicates that the -SO_3 can optimize the structure of ZnS and enhance the stability of ZnS@SO_3 SEI. More solid evidence can be obtained as shown in Figure 3e and Figure S24, respectively, where the Zn^{2+} plating/stripping efficiency can be improved to an average CE (ACE) of 99.55 % over 1790 cycles at a current density of 5 mA cm^{-2} and a capacity of 1 mAh cm^{-2} (Figure 3e). In contrast, the bare Zn electrode shows a poor plating/stripping efficiency within only 320 cycles because of a short circuit, which further demonstrates the enhancement of -SO_3 anion in promoting interfacial modification. Following, the Zn reversibility behavior was also investigated at 2 mA cm^{-2} and

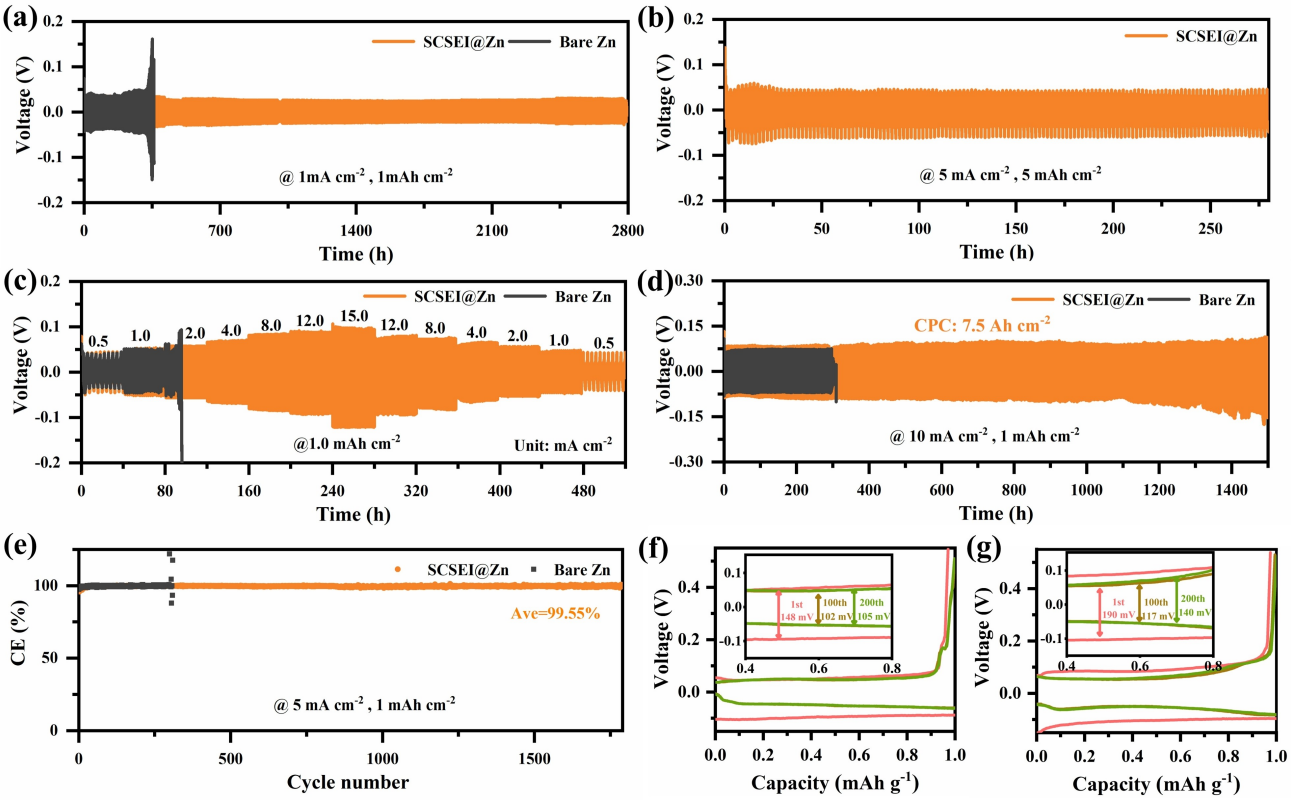

Figure 3. Cycling performance of symmetric Zn//Zn cells in bare Zn and SCSEI@Zn at (a) 1 mA cm^{-2} for 1 mAh cm^{-2} (b) 5 mA cm^{-2} for 5 mAh cm^{-2}. (c) Rate performance at various current densities (d) 10 mA cm^{-2} for 1 mAh cm^{-2}. (e) CE of Zn//Cu cells. Corresponding voltage profiles of the Zn//Cu cells at different cycles in (f) SCSEI@Zn. (g) Bare Zn.

2 mAh cm^{-2} (Figure S24), the asymmetrical cells with SCSEI@Zn electrodes show a higher initial Coulombic efficiency (ICE) of 97.6 % and a high ACE of 99.6 %, which is much higher than that of bare Zn electrode.

To elucidate the reasons for why SCSEI@Zn electrodes can effectively enhance the electrochemical performance, a three-electrode system has been adopted to systematically study the regulation and protection mechanism of SCSEI@Zn during plating/stripping. Chronoamperometry curves have been adopted as the critical method to understand the nucleation and surface change mechanisms of the diffusion mechanism of Zn^{2+}. The SCSEI@Zn electrode shows faster 2D diffusion time and lower 3D diffusion response current density than the bare Zn electrode during the testing under a constant overpotential −150 mV (Figure 4a). In contrast, with a bare Zn electrode, Zn^{2+} ions diffuse laterally along the surface during 2D diffusion, leading to the 'tip effect' and subsequent harmful dendrite growth (Figure S25).[20] On the other hand, in the SCSEI@Zn electrode, the current of 3D diffusion is significantly reduced, promoting smooth Zn deposition and preventing charge accumulation during the 3D diffusion. These phenomena demonstrate that SCSEI@Zn electrode is more effective in guiding uniform Zn^{2+} deposition compared to a bare Zn electrode.

Linear sweep voltammetry (LSV) curves were performed in different electrodes (Figure 4b). It is obvious that the introduction of SCSEI layer results in a much lower hydrogen evolution potential (−1.121 V vs. Ag/AgCl) than the bare Zn electrode (−1.063 V vs. Ag/AgCl). Subsequently, the corrosion current density decreases from 0.35 mA cm^{-2} of bare Zn electrode to 0.14 mA cm^{-2} of SCSEI@Zn electrode (Figure 4c). The reduced HER potential and corrosion current further confirm that SCSEI@Zn electrode has the effect of inhibiting chemical corrosion.[21] At the same time, the evolution of surface morphologies after deposition has also been characterized, referring to the morphology of the initial Zn anodes in Figure S26. The surface of the bare Zn anode is covered by flake-like dendrites and some hexagonal byproducts after 20 cycles (Figures 4d and 4e). Nevertheless, the surface of SCSEI@Zn anode still shows a very smooth and dense feature at different magnifications after the deposition of Zn^{2+} (Figure 4h and 4g). More detailed morphologies can be observed in the 3D confocal microscope image (Figure S27). The SCSEI@Zn shows a more uniform deposition than that using a bare Zn electrode at 1 mA cm^{-2}/1 mAh cm^{-2} after 20 cycles, this indicates that the SCSEI can efficiently inhibit the dendrite growth, thus inducing a uniform Zn deposition. A more vivid electroplating process can be directly observed from the real-time in situ optical microscopy (Figure 4h and 4i). During the electrodeposition within the bare Zn electrode, several loose and random aggregations and protuberances emerge after 20 min and continuously grow

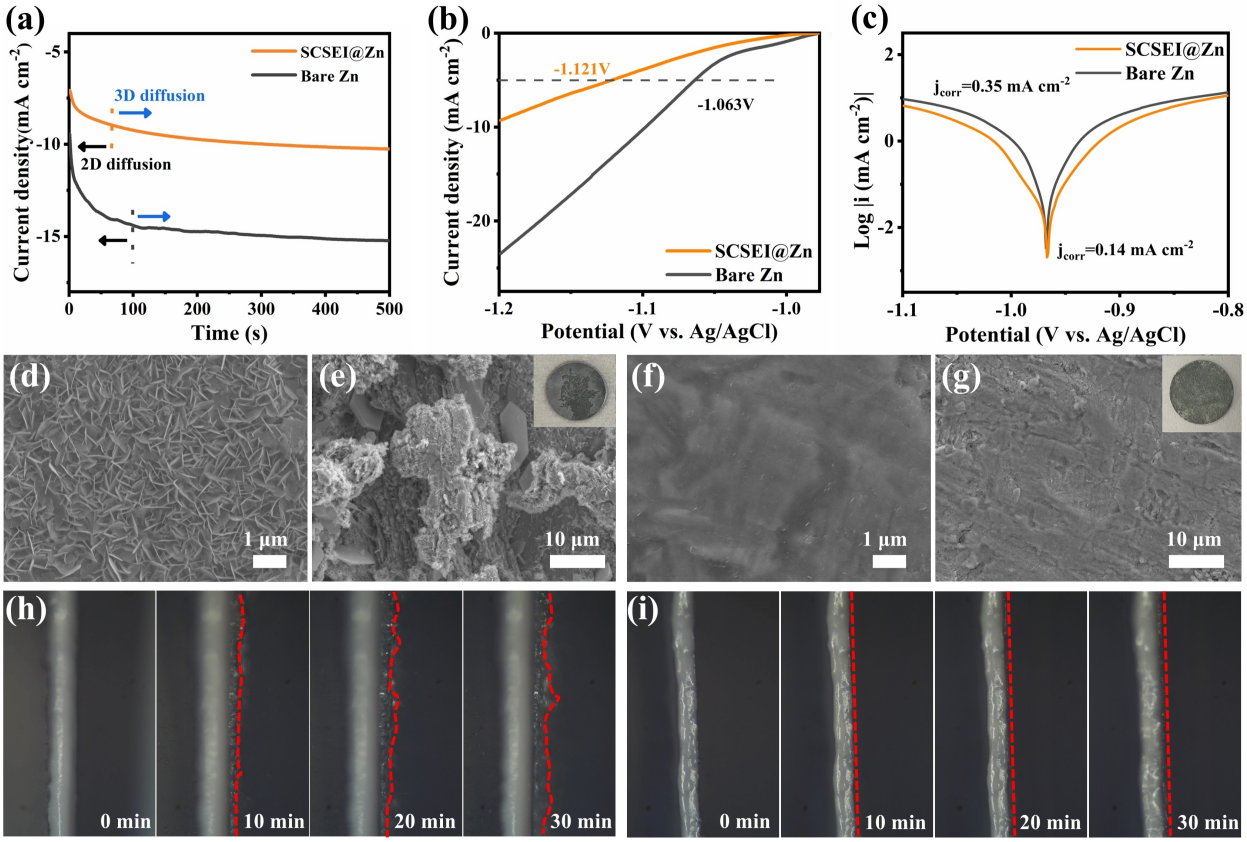

Figure 4. Three-electrode system with SCSEI@Zn and bare Zn electrodes. (a) Chronoamperometry curves at a constant potential of −150 mV. (b) Comparison of HER performance energies and (c) Tafel plots of Zn//Zn symmetric cells. The SEM image of the Zn deposited with (d–e) bare Zn and (f–g) SCSEI@Zn electrodes at 1 mAh cm^{-2} for 20 cycles. Insets are optical photos of corresponding samples. In situ optical microscopic observations of the Zn surface with (h) bare Zn and (i) SCSEI@Zn electrode.

into irreversible dendrites. On the contrary, the SCSEI@Zn electrode shows a smoother surface and a tighter layer of deposition (marked with a dotted line), suggesting the uniform deposition behavior of Zn^{2+}, which is in line with the above results.

In the following, the stepwise dehydration energy of $Zn(H_2O)_x^{2+}$ ($x=0$–6, integer) was simulated by DFT calculations to clarify the impact of ZnS@SO_3 on the dehydration process. As previously reported, the original Zn^{2+} cations commonly coordinate with six surrounding water molecules to form $[Zn(H_2O)_6]^{2+}$ in an aqueous electrolyte.[12a,22] In this case, the Zn^{2+} needs to escape from the solvation shell by breaking the Zn^{2+}-H_2O bonds ($[Zn(H_2O)_6]^{2+} \rightarrow Zn^{2+} + 6H_2O$) before diffusing into the host structure. Benefiting from the interaction between -SO_3 and active water molecules (derived from $[Zn(H_2O)_6]^{2+}$), the process of dehydration of ZnS@SO_3 is significantly accelerated (Figure 5a). Especially, when six water molecules are derived from the $[Zn(H_2O)_6]^{2+}$, the dehydration energy of ZnS@SO_3 is only 3.52 eV which is much lower than that of pure ZnS (5.25 eV). This indicates that -SO_3 anion can facilitate the desolvation of hydrated Zn^{2+} and promote the Zn^{2+} diffusion via bridging -SO_3 onto ZnS with a lower energy barrier. On the one hand, the -SO_3 molecules endow the richness in oxygen-containing functional groups in the SCSEI layer, which can serve as hydrogen bonding acceptor. On the other hand, these unsaturated oxygen groups in -SO_3 molecules are zincophilic functional group, and preferentially work as the "oxygen ferry" between ZnS and Zn^{2+}, contributing to capturing Zn^{2+} and enhancing the strong interaction of Zn–O bonding network. The detailed diffusion path is illustrated (Figure 5b). In contrast, there is no obvious interaction between Zn^{2+} and ZnS along the ZnS diffusion path (Figure S28). These results clearly indicate that the structure of ZnS@SO_3 not only achieves fast Zn^{2+} desolvation ability but also effectively suppresses the uneven diffusion of Zn^{2+}, giving rise to uniform Zn deposition.

Furthermore, the stability of the ZnS/Zn interface and homogenization of the ZnS/Zn interface electric field are also explored by DFT calculations. As shown in the charge density difference at the Zn/ZnS@SO_3 SCSEI interphase (Figure 5c and 5d), due to the existence of unsaturated chemical bond ("O" derived from -SO_3) exposing at the in situ ZnS@SO_3 out layer, the electrons rearrange at the Zn/ZnS interface, a built-in electric field is formed that not only maintains interfacial stability but also effectively promotes the reversible diffusion of Zn^{2+}. Further solid experimental evidence supports the role of -SO_3 in promoting Zn^{2+} dynamic kinetics. Activation energy measurements show that the bare Zn anode exhibits a high value of

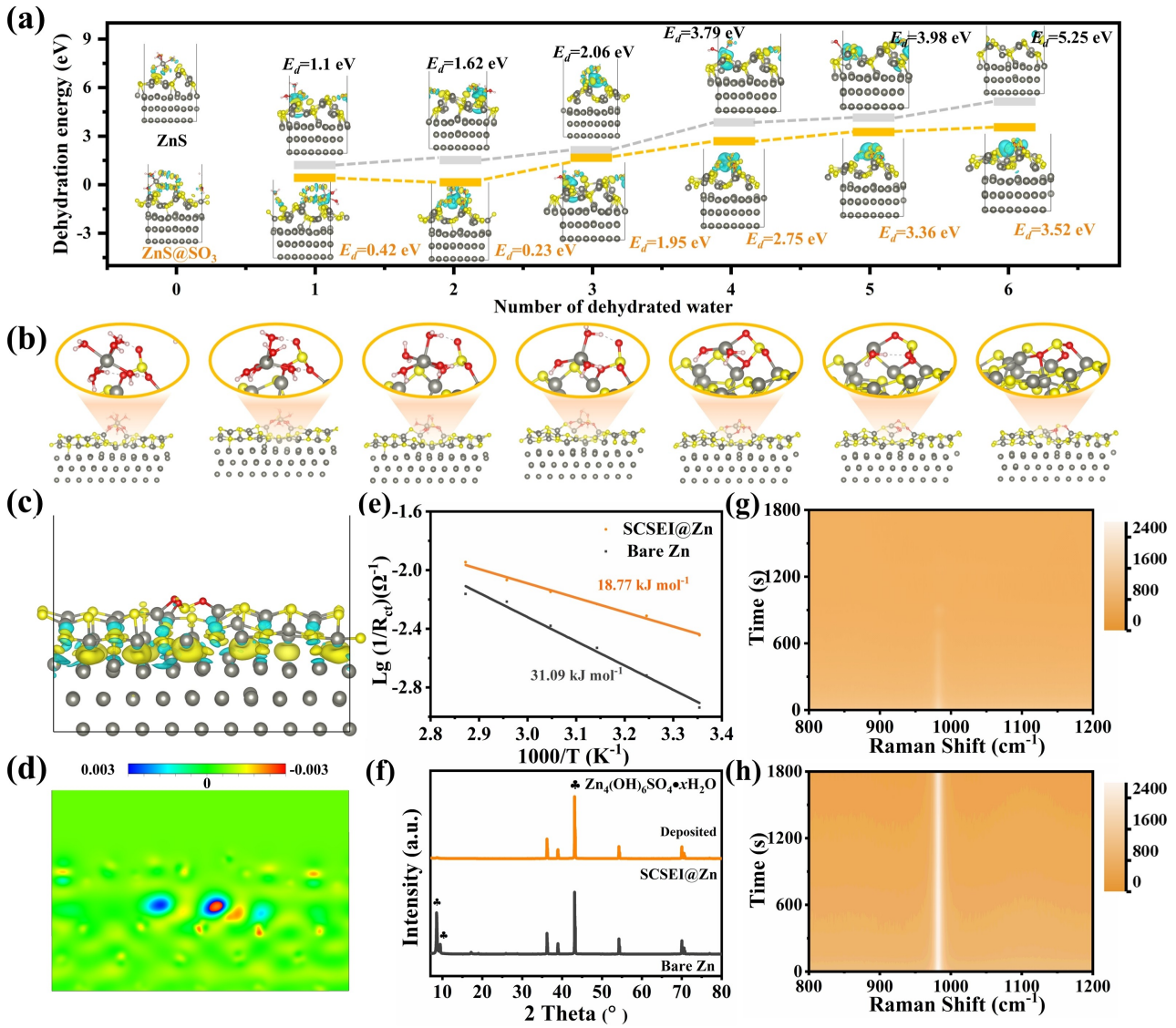

Figure 5. Theoretical understanding of the Zn dehydration and diffusion mechanism. (a) Stepwise dehydration energies of Zn with ZnS@SO_3. Insets: molecular geometries corresponding to the dehydration of $Zn(H_2O)_x^{2+}$. (b) The migration process of Zn^{2+} with ZnS@SO_3. (c) The differential charge density diagram of ZnS@ SO_3 and (d) 2D contour map of electron density. (e) Arrhenius curves using SCSEI@Zn and bare Zn electrode. (f) XRD patterns of Zn metal after cycling with SCSEI@Zn and bare Zn electrode at a current density of 1 mA cm^{-2}. In situ Raman spectra of the surface layer of the working electrode with (g) SCSEI@Zn and (h) bare Zn.

31.09 kJ mol^{-1}, while the value drops significantly to 18.77 kJ mol^{-1} of that using SCSEI@Zn anode. This reduction is consistent with the ability of the ZnS@SO_3 layer to promote the dehydration of $[Zn(H_2O)_6]^{2+}$, therefore enhancing Zn^{2+} transport kinetics and uniform deposition during the cycling process (Figure 5e). Additional, X-ray diffraction (XRD) patterns (Figure 5f) reveal that there is no obvious harmful by-product (ZSH) on the surface of SCSEI@Zn electrode after 20 cycles, indicating the effective suppression of side reactions of Zn in the aqueous electrolyte.[5a] In situ Raman spectrum was employed to monitor the evolution of the characteristic vibration peak at 980 cm^{-1} (ν-SO_4^{2-}), corresponding to the zinc hydroxyl sulfate by-product.[9b,15,23] The intensity decreases gradually with the increase of the deposition time within the SCSEI@Zn electrode (Figure 5g). In contrast, there are no significant changes in the peak intensity of SO_4^{2-} within the bare Zn electrode (Figure 5h). Clearly, the existence of -SO_3 distributing on the Zn surface after forming the ZnS@SO_3 protective layer can create the accumulation of negative charges on the surface, causing the repulsion effect and the effective inhibition of the by-product and corrosion reactions.

The effects of ZnS@SO_3 layer on the applicability of a full zinc-ion battery have been investigated (Figure 6). In detail, we employed homemade ammonium vanadium oxide ($NH_4V_4O_{10}$, NVO) cathode and analyzed the electrochemical performance in the voltage of 0.4–1.4 V (Figures S29 and S30). The full cells using SCSEI@Zn electrode exhibit a stable discharge capacity of 207.9 mAh g^{-1} after 2000 cycles (~1.24-fold of that using bare Zn electrode) together with a

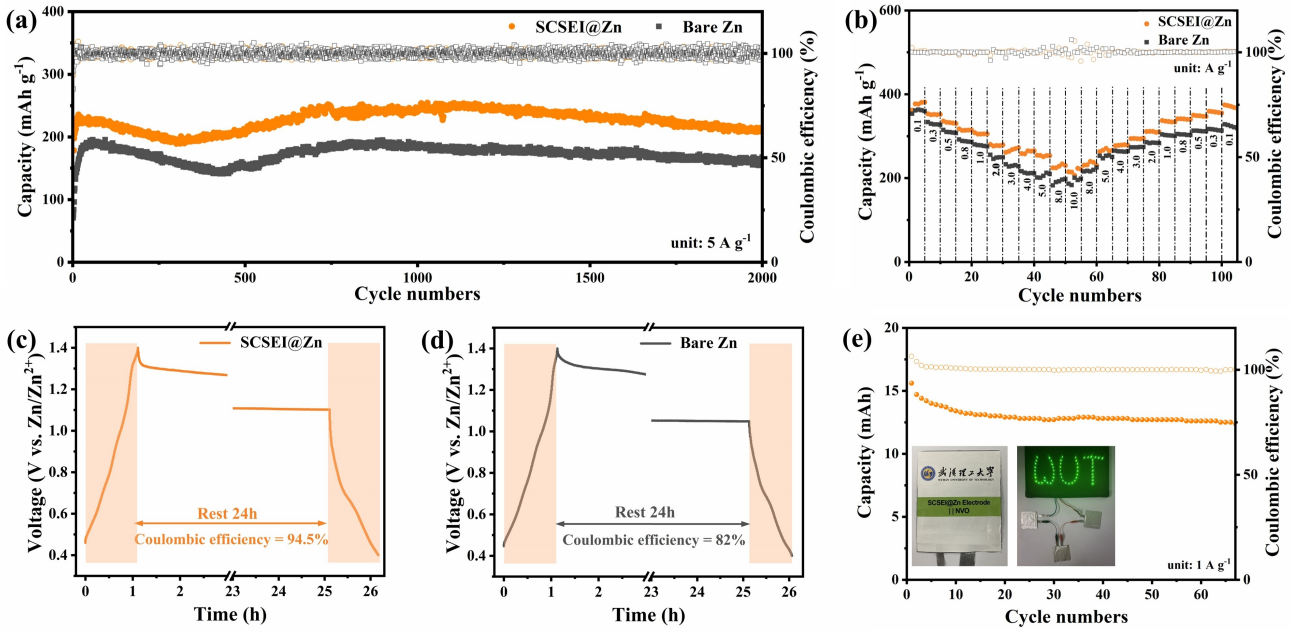

Figure 6. The Zn//NVO full cell performance with SCSEI@Zn and bare Zn anodes. (a) Cycling performance at 5 $A g^{-1}$. (b) Rate performance. Self-discharge test of the Zn || NVO cells using (c) SCSEI@Zn and (d) bare Zn anodes. (e) Cycling performance at 1 $A g^{-1}$ of the Zn || NVO pouch cells with SCSEI@Zn anode. (Insets are the electrodes and the optical photos of Zn || NVO pouch cells).

high CE of nearly 100 % after 2000 cycles. Meanwhile, the full cell with SCSEI@Zn electrode exhibits a superior rate capability (Figure 6b). Specifically, the full cell using SCSEI@Zn electrode delivers higher capacities of 375.4 to 236.8 $mAh g^{-1}$ at the rates of 0.1 $A g^{-1}$ to 10 $A g^{-1}$, than that of the full cell with bare Zn electrode at various current densities. Besides, the corresponding charge–discharge curves of rate performances (Figure S31). It is clear that the overpotential of the full cell after introducing the SCSEI layer on Zn anode is significantly reduced. In addition, to minimize process error, self-discharging measurements were taken for full cells activated for several cycles at 0.3 $A g^{-1}$ using two different electrolytes. The self-discharge curves of the full cell show that SCSEI@Zn anode effectively enhances the electrochemical performance, with CE improved from 82 % to 94.5 % (Figure 6c and 6d). To demonstrate the concept further, a pouch-type full cell using SCSEI@Zn electrode exhibits prominent cycle stability at 1 $A g^{-1}$ for 65 cycles (Figure 6e).

Conclusion

In this work, we have explored and revealed the electrochemical new role of $-SO_3$ and ZnS in the in situ formed SEI on Zn anode electrochemistry in $ZnSO_4$ aqueous electrolytes. After introducing Flu additives into the electrolyte, a sulfurized composite solid electrolyte interphase (SCSEI) layer can be in situ formed on the Zn anode interface after cycling. The $-SO_3$ adsorbed on the surface of ZnS not only stabilizes the interaction between ZnS and Zn anode, but also reduces the dehydration energy of $[Zn(H_2O)_6]^{2+}$, significantly accelerating the dynamic kinetics of Zn^{2+}. Moreover, the ZnS composite SEI layer shows effective suppression of side reactions, and the electronic rearrangement at the ZnS/Zn interface introduces a built-in electric field that promotes the rapid diffusion of dehydrated Zn^{2+} into the interlayer of ZnS/Zn, thus promoting Zn^{2+} uniform deposition during cycling. Owing to the synergistic effect of ZnS and $-SO_3$, a symmetrical cell exhibits an excellent cycling stability of over 1500 h with a high cumulative-plated capacity of 7.5 $mAh cm^{-2}$ at 10 $mA cm^{-2}$. Impressively, the asymmetrical cell delivers a high average CE of 99.55 % over 1790 cycles. Moreover, Zn || NVO full cell at 5 $A g^{-1}$ achieves excellent cycling stability (2000 cycles and CE nearly 100 %). These new findings not only highlight the universal method for achieving high-performance AZIBs but also provide new insights into anionic synergistic effects on the electrochemical plating/stripping behavior of Zn ions.

Acknowledgements

This work was supported by the National Natural Science Foundation of China (Nos. 52272234, 51832004), the China Postdoctoral Science Foundation (No. 2024M752495), the Postdoctoral Fellowship Program of CPSF (No. GZB20230552), the National Key Research and Development Program of China (No. 2020YFA0715000), the International Science and Technology Cooperation Program of Hubei Province (No. 2024EHA039), the Independent Innovation Projects of the Hubei Longzhong Laboratory (No. 2022ZZ-20), the Sanya Science and Education Innovation Park of Wuhan University of Technology (No.

2021KF0011), the Postgraduate Innovation Foundation of Wuhan University of Longzhong Laboratory (No. 2023XY-Z-001) and the Italy-Singapore Science and Technology Cooperation Program (No. R22I0IR121).

Conflict of Interest

The authors declare no conflict of interest.

Data Availability Statement

The data that support the findings of this study are available from the corresponding author upon reasonable request.

Keywords: electrolyte · in situ sulfurized SEI · anionic synergistic · zinc ion batteries

[1] a) S. Ha, K. Tae Lee, *Nat. Energy* **2016**, *1*, 16057; b) X. Zeng, J. Mao, J. Hao, J. Liu, S. Liu, Z. Wang, Y. Wang, S. Zhang, T. Zheng, J. Liu, P. Rao, Z. Guo, *Adv. Mater.* **2021**, *33*, 2007416; c) X. Yang, C. Li, Z. Sun, S. Yang, Z. Shi, R. Huang, B. Liu, S. Li, Y. Wu, M. Wang, Y. Su, S. Dou, *J. Sun, Adv. Mater.* **2021**, *33*, 2105951; d) Z. Xing, Y. Sun, X. Xie, Y. Tang, G. Xu, J. Han, B. Lu, S. Liang, G. Chen, J. Zhou, *Angew. Chem. Int. Ed.* **2023**, 62; e) F. Xiong, Y. Jiang, L. Cheng, R. Yu, S. Tan, C. Tang, C. Zuo, Q. An, Y. Zhao, J. J. Gaumet, *Interdiscip. Mater.* **2022**, *1*, 140–147.

[2] a) L. Ma, M. A. Schroeder, O. Borodin, T. P. Pollard, M. S. Ding, C. Wang, K. Xu, *Nat. Energy* **2020**, *5*, 743–749; b) C. Li, A. Shyamsunder, A. G. Hoane, D. M. Long, C. Y. Kwok, P. G. Kotula, K. R. Zavadil, A. A. Gewirth, L. F. Nazar, *Joule* **2022**, *6*, 1103–1120; c) H. Kim, S.-H. Lee, J.-M. Kim, C. S. Yoon, Y.-K. Sun, *ACS Energy Lett.* **2023**, *8*, 2970–2978.

[3] a) S. Yang, A. Chen, Z. Tang, Z. Wu, P. Li, Y. Wang, X. Wang, X. Jin, S. Bai, C. Zhi, *Energy Environ. Sci.* **2024**, *17*, 1095–1106; b) Y. Zhong, X. Xie, Z. Zeng, B. Lu, G. Chen, J. Zhou, *Angew. Chem. Int. Ed.* **2023**, *62*, e202310577; c) Z. Gong, Z. Li, P. Wang, K. Jiang, Z. Bai, K. Zhu, J. Yan, K. Ye, G. Wang, D. Cao, *Energy Mater. Adv.* **2023**, 4; d) L. Zhang, J. Xiao, X. Xiao, W. Xin, Y. Geng, Z. Yan, Z. Zhu, *eScience* **2023**, *4*, 100205.

[4] a) Y. Liu, J. Wang, J. Sun, F. Xiong, Q. Liu, Y. An, L. Shen, J. Wang, Q. An, L. Mai, *J. Mater. Chem. A* **2022**, *10*, 25029–25038; b) S. Chen, D. Ji, Q. Chen, J. Ma, S. Hou, J. Zhang, *Nat. Commun.* **2023**, *14*, 3526.

[5] a) J. Cao, D. Zhang, X. Zhang, Z. Zeng, J. Qin, Y. Huang, *Energy Environ. Sci.* **2022**, *15*, 499–528; b) J. Zhu, Z. Tie, S. Bi, Z. Niu, *Angew. Chem. Int. Ed.* **2024**, e202403712.

[6] C. Li, G. Qu, X. Zhang, C. Wang, X. Xu, *Energy Environ. Materials* **2023**, e12608.

[7] J. Hao, B. Li, X. Li, X. Zeng, S. Zhang, F. Yang, S. Liu, D. Li, C. Wu, Z. Guo, *Adv. Mater.* **2020**, *32*, 2003021.

[8] a) Y. Li, Z. Yu, J. Huang, Y. Wang, Y. Xia, *Angew. Chem. Int. Ed.* **2023**, *62*, e202309957; b) X. Cao, W. Xu, D. Zheng, F. Wang, Y. Wang, X. Shi, X. Lu, *Angew. Chem. Int. Ed.* **2024**, *63*, e202317302.

[9] a) Z. Yang, Y.-L. Sun, S. Deng, H. Tong, M. Wu, X. Nie, Y. Su, G. He, Y. Zhang, J. Li, *Energy Environ. Sci.* **2024**; b) Y. Lv, M. Zhao, Y. Du, Y. Kang, Y. Xiao, S. Chen, *Energy Environ. Sci.* **2022**, *15*, 4748–4760; c) C. Huang, F. Huang, X. Zhao, Y. Hao, Y. Yang, Y. Qian, G. Chang, Y. Zhang, Q. Tang, A. Hu, *Adv. Funct. Mater.* **2023**, *33*.

[10] a) Z. Jiao, X. Cai, X. Wang, Y. Li, Z. Bie, W. Song, *Adv. Energy Mater.* **2023**, *13*, 2302676; b) P. Sun, L. Ma, W. Zhou, M. Qiu, Z. Wang, D. Chao, W. Mai, *Angew. Chem. Int. Ed.* **2021**, *60*, 18247–18255.

[11] a) C. Zhou, C. Dong, W. Wang, Y. Tian, C. Shen, K. Yan, L. Mai, X. Xu, *Interdiscip. Mater.* **2024**, *3*, 306–315; b) H. Xu, C. Sun, S. Zhang, H. Zhang, Z. Liu, Y. Tang, G. Cui, *ChemSusChem* **2023**, *16*, e202202334.

[12] a) Y. Liu, S. Chen, H. Yuan, F. Xiong, Q. Liu, Y. An, J. Zhang, L. Wu, J. Sun, Y.-W. Zhang, *Sci. Bull.* **2023**, *68*, 2993–3002; b) C. Chang, S. Hu, T. Li, F. Zeng, D. Wang, S. Guo, M. Xu, G. Liang, Y. Tang, H. Li, Energy *Environ. Sci.* **2024**, *17*, 680–694.

[13] a) D. Xie, Y. Sang, D. H. Wang, W. Y. Diao, F. Y. Tao, C. Liu, J. W. Wang, H. Z. Sun, J. P. Zhang, X. L. Wu, *Angew. Chem. Int. Ed.* **2023**, *62*; b) M. Wu, X. Wang, F. Zhang, Q. Xiang, Y. Li, J. Guo, *Energy Environ. Sci.* **2024**, *17*, 619–629.

[14] L. Ma, Q. Li, Y. Ying, F. Ma, S. Chen, Y. Li, H. Huang, C. Zhi, *Adv. Mater.* **2021**, *33*.

[15] A. Zhou, H. Wang, X. Hu, F. Zhang, Y. Zhao, Z. Hu, Q. Zhang, Z. Song, Y. Huang, L. Li, *Sci. Bull.* **2023**, *68*, 2170–2179.

[16] Y. Liu, Y. An, L. Wu, J. Sun, F. Xiong, H. Tang, S. Chen, Y. Guo, L. Zhang, Q. J. A. An, *ACS Nano* **2022**, *17*, 552–560.

[17] A. Zhou, H. Wang, X. Hu, F. Zhang, Y. Zhao, Z. Hu, Q. Zhang, Z. Song, Y. Huang, L. Li, F. Wu, R. Chen, *Sci. Bull.* **2023**, *68*, 2170–2179.

[18] a) M. Peng, X. Tang, K. Xiao, T. Hu, K. Yuan, Y. Chen, *Angew. Chem. Int. Ed.* **2023**, *62*, e202302701; b) W. Xu, J. Li, X. Liao, L. Zhang, X. Zhang, C. Liu, K. Amine, K. Zhao, J. Lu, *J. Am. Chem. Soc.* **2023**, *145*, 22456–22465.

[19] J. Yang, R. Zhao, Y. Wang, Y. Bai, C. Wu, *Energy Mater. Adv.* **2022**, *2022*, 9809626.

[20] Q. Jiao, X. Zhai, Z. Sun, W. Wang, S. Liu, H. Ding, W. Chu, M. Zhou, C. Wu, *Adv. Mater.* **2023**, *35*, 2300850.

[21] Y. Yang, C. Liu, Z. Lv, H. Yang, Y. Zhang, M. Ye, L. Chen, J. Zhao, C. C. Li, *Adv. Mater.* **2021**, *33*, 2007388.

[22] H. Du, R. Zhao, Y. Yang, Z. Liu, L. Qie, Y. Huang, *Angew. Chem. Int. Ed.* **2022**, *61*, e202114789.

[23] W. Zhang, Y. Lu, L. Wan, P. Zhou, Y. Xia, S. Yan, X. Chen, H. Zhou, H. Dong, K. Liu, *Nat. Commun.* **2022**, *13*, 2029.

Manuscript received: October 9, 2024
Accepted manuscript online: November 11, 2024
Version of record online: November 21, 2024